Array-based seismic measurements of OSIRIS-REx's re-entry

Benjamin A. Fernando[1], Constantinos Charalambous[2], Nick Schmerr[3], Timothy J. Craig[4], Jonathan Wolf[5], Kevin Lewis[1], Eleanor K. Sansom[6,7], Christelle Saliby[8], Meaghan McCleary[9], Jennifer Inman[10], Justin LaPierre[11], Miro Ronac Giannone[12], Karen Pearson[13], Michael Fleigle[14], Carene Larmat[15], Ozgur Karatekin[16], Lavender Elle Hanson[1], Shivani Baliyan[17], David Buttsworth[18], Hiu Ching Jupiter Cheng[19], Neeraja S. Chinchalkar[20], Luke Daly[21], Hadrien A. R. Devillepoix[4], Aly Muhammad Gajani[22], Carina T. Gerritzen[23], Harish[24], Daniel C. Hicks[25], Roy Johnson[26], Sabrina Y. Khan[1], Sarah N. Lamm[27], Cara Pesciotta[1], Tom Rivlin[28], Lucie Rolland[29], Maxwell Marzban Thiemens[30], Alice R. Turner[31], and Fabian Zander[18]

Cite this article as (2022). Array-based seismic measurements of OSIRIS-REx's re-entry, *Seismol. Res. Lett.* **XX**, 2–19, doi: .

Supplemental Material

Abstract

The return home of the OSIRIS-REx spacecraft in September 2023 marked only the fifth time that an artificial object entered the Earth's atmosphere at interplanetary velocities. Although rare, such events serve as valuable analogues for natural meteoroid re-entries; enabling study of hypersonic dynamics, shockwave generation, and acoustic-to-seismic coupling. Here, we report on the signatures recorded by a dense (100-m scale) 11-station array located almost directly underneath the capsule's point of peak atmospheric heating in northern Nevada. Seismic data are presented which allow inferences to be made about the shape of the shockwave's footprint on the surface, the capsule's trajectory, and its flight parameters.

Introduction

Sample return capsules and seismoacoustics

Sample return capsules arriving from deep space are the only artificial objects which re-enter the Earth's atmosphere at speeds and trajectories comparable to natural meteoroids. This makes them ideal for studying hypersonic re-entry dynamics as said

*Corresponding author: bfernan9@jh.edu

capsules have known mass, dimension, speed, and trajectory (Silber et al., 2023). Because they have known parameters, they can serve as controlled analogues for natural objects during the EDL (Entry, Descent, and Landing) phase of the mission.

In seismoacoustic studies of meteor phenomena, the atmospheric shockwaves and low-frequency sound produced by natural meteoroids re-entering the atmosphere are used to identify and track them on either infrasound sensors or seismometers (e.g. Edwards et al. (2008)). The complexities of shockwave generation and propagation down through the turbulent atmosphere (and coupling into the ground in the case of seismic recordings) mean that recordings of hypersonic capsules acting as 'artificial meteoroids' are particularly valuable in understanding the seismoacoustic processes involved.

Such events are rare, having occurred only four times on Earth previously. ReVelle et al. (2005) made seismic and acoustic measurements of NASA's Genesis spacecraft's EDL, and ReVelle and Edwards (2007) did the same for NASA's Stardust. More recently, comparable measurements were made during the EDLs of two JAXA missions, Hayabusa and Hayabusa2 (Yamamoto et al., 2011; Sansom et al., 2022).

The potential value of such recordings for being able to study shockwave propagation and air-to-ground coupling in particular also resulted in two (unsuccessful) attempts by NASA's InSight spacecraft to record EDLs seismoacoustically on Mars, of NASA's Mars 2020 mission (Fernando et al., 2021, 2022) and China's Tianwen-1 (Fernando et al., 2021).

The OSIRIS-REx mission

In September 2023, the OSIRIS-REx (ORX) sample return capsule became the fifth artificial object to re-enter the Earth's atmosphere at interplanetary speeds. With many improvements in instrumentation having been made since Stardust's landing in 2006, the ORX EDL presented an ideal opportunity to make seismoacoustic measurements of an 'artificial meteoroid' re-entry over a similar geographical area to two previous missions.

A number of different teams took part in this instrumentation campaign, using both ground-based and airborne infrasound sensors, and conventional and optical seismometers. For a full review of the instruments deployed as part of this campaign see Silber et al. (2024). Fernando et al. (2024) presented initial results from a separate part of this observation campaign, using a single seismic-acoustic station 50 km from the array described in this paper at a site called Fish Creek from which the data was live-streamed over the internet.

EDL profile

In this section, we briefly describe the planned trajectory of ORX between atmospheric interface and peak heating. Note that all times and locations are based on pre-landing model predictions (e.g. Ajluni et al. (2015)), as a post-landing 'as-flown' trajectory has not yet been released.

Atmospheric interface was due to occur over the Pacific Ocean, west of San Francisco, California at 14:41:55 UTC on Sunday, 2023-09-24. The defined altitude of interface was 132 km, at which time the spacecraft was expected to be travelling at approximately Mach 25 (43,000 km/h; 11.9 km/s).

At the point of peak atmospheric heating from frictional drag, the capsule was expected to be in the mesosphere at around 62 km altitude over 39.5585°N, 116.3852°W in northern Nevada. This is a relatively remote region with no permanent seismometers within several dozen kilometres, and we are not aware of any publicly accessible infrasound stations within the wider area. This necessitated deployment of these temporary seismic arrays.

Temperatures during peak heating were expected to reach approximately 3100 K at a speed of Mach 30 (39,000 km/h; 10.8 km/s) and a deceleration approaching 300 m/s^2 (31 g). Note that the Mach number at peak heating is actually higher than at atmospheric interface despite the capsule's deceleration, due to the increase in sound speed with altitude through the thermosphere.

As the point of peak heating is where the maximum amount of energy is being dissipated into the atmosphere, the expectation was for an intense shockwave to be generated in this area. This shock was expected to transition to a linear acoustic wave during propagation down through the atmosphere and be audible at the surface as a sonic boom.

On a seismic network, the sonic booms themselves are primarily recorded via the production of an itinerant strain field in response to the surface loading and unloading from wavefront-induced compression and rarefaction (Kanamori et al., 1992). Small contributions to the observed displacement after the initial motion may also come about from more complex effects, such as compliance-induced ground deformation (Sorrells, 1971; Kenda et al., 2020).

Instrumentation campaign

The deployment discussed in this paper involved eleven individual seismic stations, each consisting of a three-axis Fairfield ZLand 3C Nodes set to 24dB gain and 2000 samples per second.

The deployment location for these nodes was chosen to be as close to the point of projected peak heating as possible, to try to capture the shockwave at its strongest point. For natural meteoroids, peak emission is expected to occur around the point of peak heating, and hence measurements made of artificial capsules in this region of flight are of particular interest as analogues.

The array was located at Bean Flats, on United States Bureau of Land Management land, in an area shared with large herbivorous creatures (cows). Despite the presence of topographic variation in the wider region, this area itself was very flat, with less than 4 m of undulation between the array's centre and edge in any direction. Given a sound-speed in air of approximately 330 m/s, this corresponds to a very small elevation-induced correction to phase arrival times, on the order of 0.01 s.

Instruments were deployed in a cross-shaped array, with an instrument spacing of approximately 100 m. This configuration, and wider geographical context, are shown in Fig. 1 alongside the ORX EDL trajectory. The long axis of the array was chosen to be parallel to ORX's trajectory footprint.

Each instrument was manually levelled and pointed toward north using multiple compasses as references, with errors in orientation estimated to be less than ±2°. The reported GPS coordinates of each station are the mean of readings made on multiple handheld instruments.

The sensors were buried with their tops a few centimetres below the ground's surface to reduce environmental noise. Some of the surface covering was removed by rain and wind (and possibly the actions of the previously mentioned herbivores) between deployment and collection. Signals from instrument 4 (the most uprange) were found to be particularly noisy. The ground at this location was ascertained to be soft, mostly dry superficial alluvium. Detailed geophysical surveys from this area of Nevada suggest soil properties described by $V_p = 585$ m/s and $V_s = 350$ m/s, Poisson ratio $\nu = 0.22$, and Young's Modulus E = 0.45 MPa (Allander and Berger, 2009).

Seismic data

Data were recorded at all eleven stations, and are shown in Fig. 2. Seismograms were processed by removing the instrument response and Butterworth-bandpass filtering between 1 and 100 Hz. The beam shown in Fig. 4 **a,b)** uses a slightly broader frequency range, 2 to 200 Hz.

Detailed N-wave structure

A clear, rounded (smoothed) N-wave signature is observed just after 14:46:04.5 UTC. A downwards, near-instantaneous first motion associated with the acoustic compression is followed by an upwards ground motion associated with the atmospheric rarefaction.

The rounding of the N-wave is characteristic of a shockwave which has decayed in the turbulent atmosphere (in particular the planetary boundary layer) to become a linear sound wave, though retaining its characteristic N-wave shape in a more rounded form (Ben-Menahem and Singh, 1981; Plotkin, 2002; Pierce and Maglieri, 1972). The arrival time is commensurate with the expected capsule overflight a few minutes previously (around 14:42 UTC). The overall duration of the N-wave phase within the wavetrain is around 0.15 s, depending on which station is examined and how the end of the rarefaction period is chosen (we use the first zero-crossing after the rarefaction).

Differences are observed in the structure of the rounded N-wave (Fig. 2), even between stations which are separated by only 100 m. Frequencies up to 500 Hz are recorded at some stations (e.g., 2 and 10), while others (e.g., 1 and 3) are limited to highest frequencies around 400 Hz. The rarefaction has a narrower frequency content than the compression, and is accordingly broader.

The most significant origins of these differences are likely propagation effects associated with inhomogeneity and turbulence in the atmosphere (Pierce and Maglieri, 1972) and local variations in sediment properties (causing different coupling behaviour, McDonald and Goforth (1969)). The spatially varying nature of the seismic source itself (i.e., the fact that the capsule is descending and decelerating over time) may also have had a small effect.

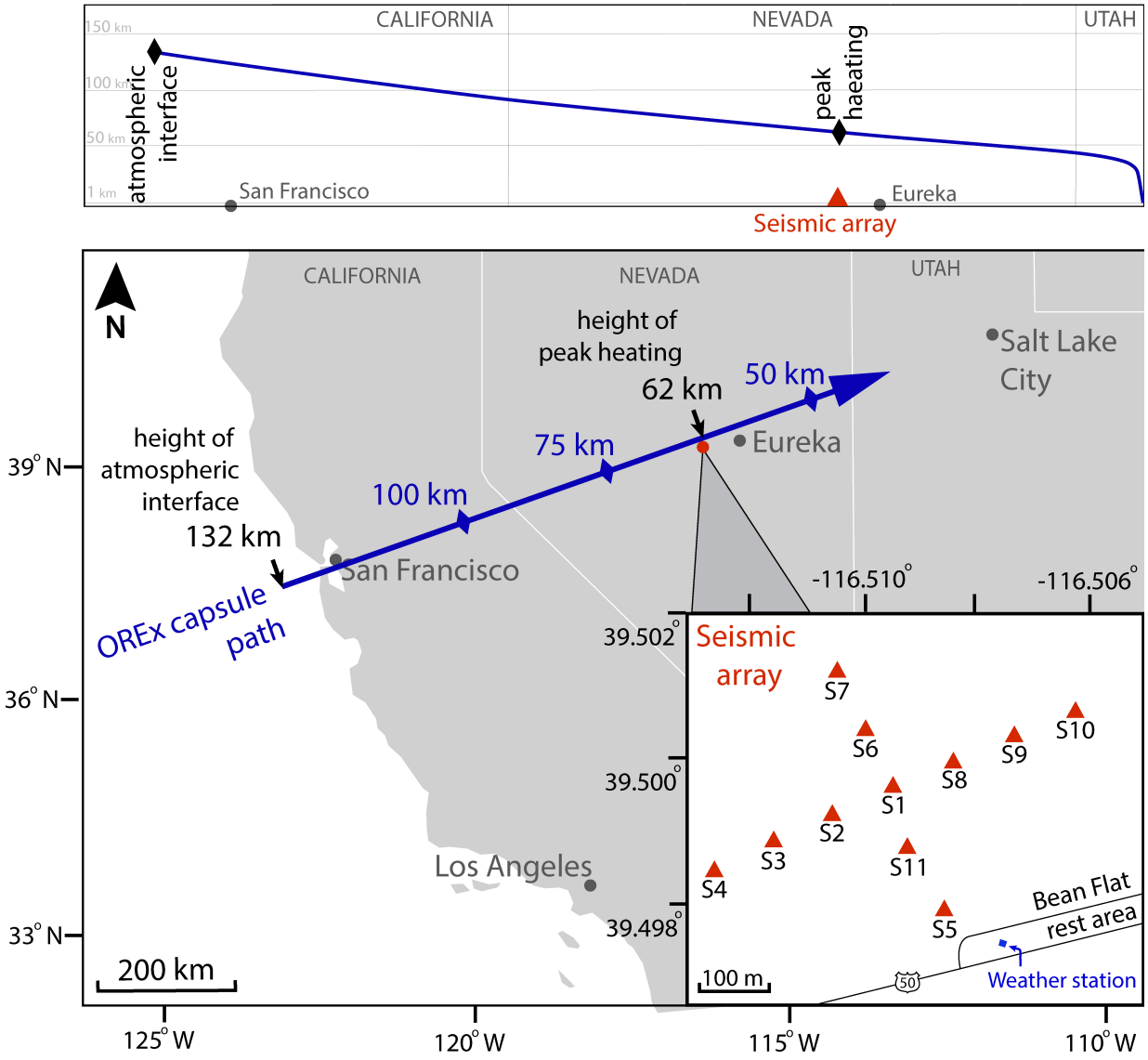

Figure 1. Top panel: the ORX EDL trajectory (side view), from the point of atmospheric interface to landing. Bottom panel: geographical context (top-down view) of the trajectory. We refer to directions towards landing as 'downrange' and those towards atmospheric interface as 'uprange'. The inset panel shows the seismometer array deployment. Note that the long arm of the array is parallel to the expected trajectory (i.e. runs uprange/downrange). The cross arm is perpendicular to the trajectory (i.e. crossrange). The lateral distance between the centre-line of the array and the trajectory footprint on the ground is approximately 2300 m.

We now consider a more detailed analysis of the signal recorded at a single station, as shown in Fig. 3. These data are for station 1, as it is located at the array centre, but similar features are recorded across the array.

As per Fig. 3**A)**, the N-wave is most clearly detectable on the vertical component, as is expected for a wavefront travelling almost vertically downward (McDonald and Goforth, 1969). A peak ground velocity of 2.6 x 10^6m/s is noted, which is slightly higher than that noted by Fernando et al. (2024) of 2.0 x 10^6 at a site 50 km away).

Fig. 3**B)** shows a vertical component spectrogram. Weak background noise, with energy predominantly at frequencies up to 30 Hz, is apparent before the rounded N-wave arrival. The amplitude variations across the array (higher noise levels closer

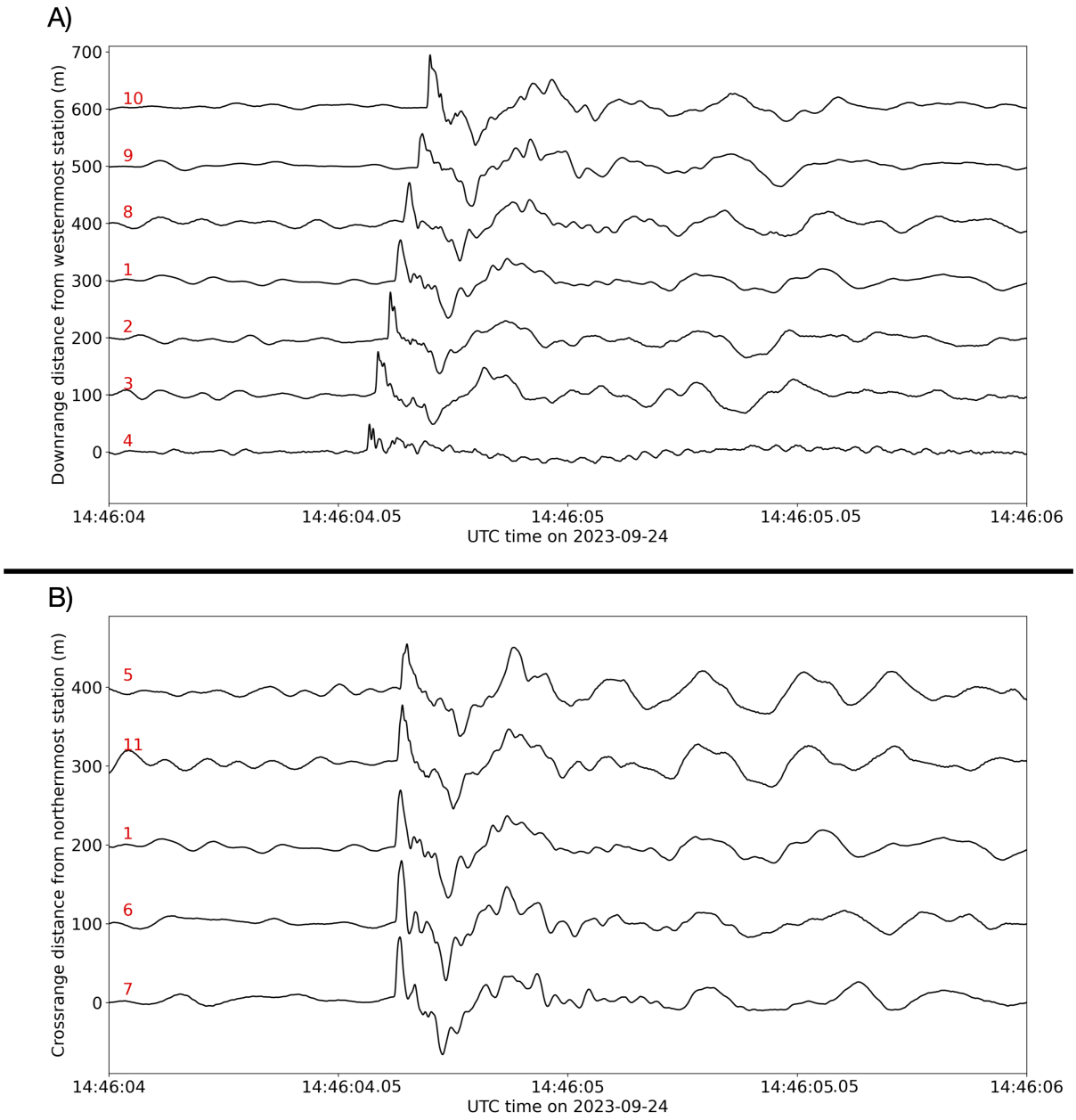

Figure 2. Seismic data recorded by the array. Traces are vertical ground velocity in the 1-100 Hz range and are arranged in **A)** by downrange distance from the westernmost station in the array and in **B)** by crossrange distance from the northernmost station. Station numbers are indicated in red on the left hand side. The weak signal at station 4 is thought to be due to issues with the instrument, which displayed higher noise levels throughout the deployment.

to the road), the move-out of the energy, and the identification of similar signatures in the seismic record at a later time (15:25-15:27 UTC) collectively indicate a vehicular origin for this particular noise source. This is discussed further in the *Traffic* section.

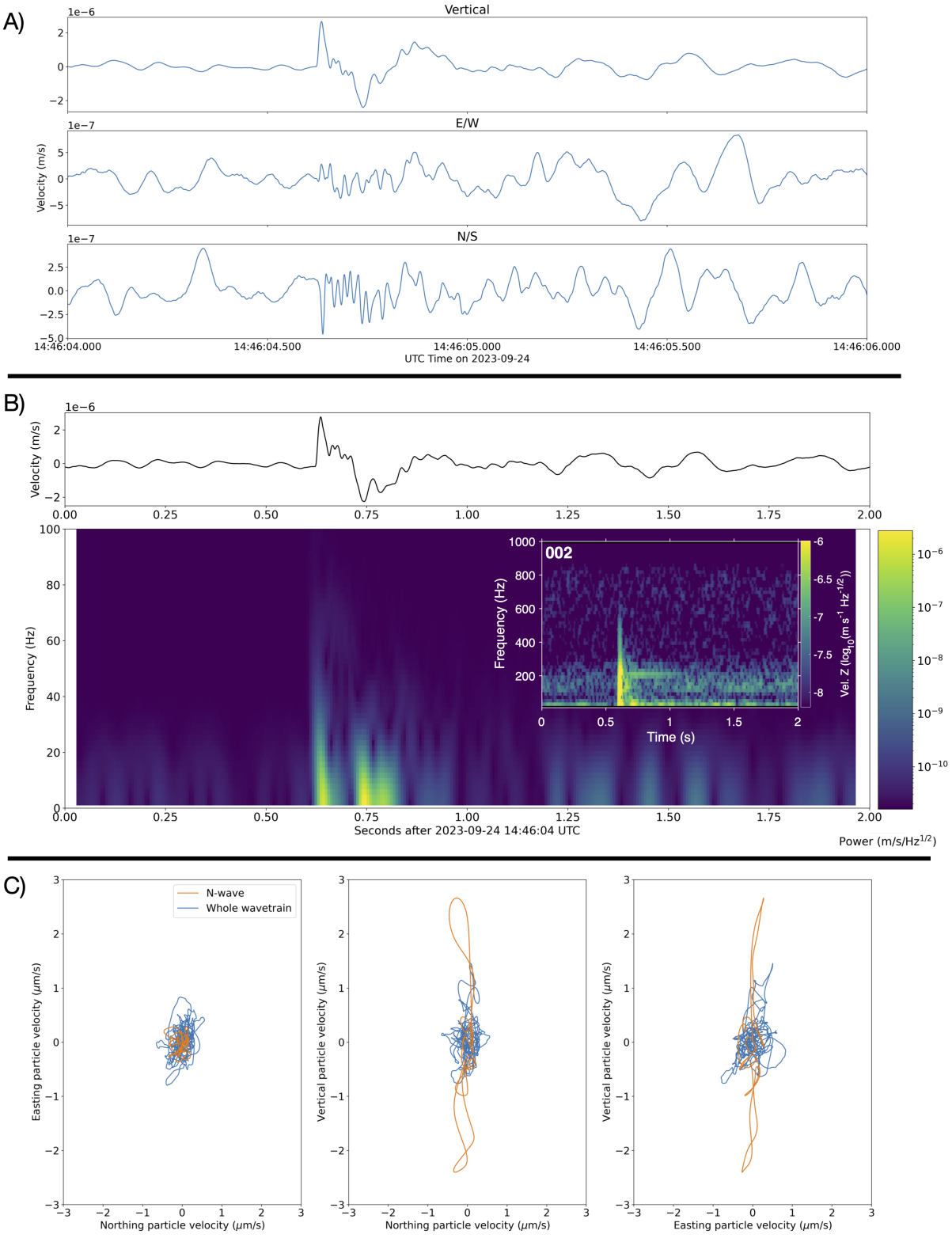

Figure 3. Data from the central station of the array (Station 1), bandpassed between 1 and 100 Hz. The N-wave is only clearly apparent on the vertical component. **A)** Three-component data, showing the dominance of the signal on the vertical component. **B)** Velocity spectrogram for the vertical component. A small inset is shown for Station 2 (one station uprange from Station 1), to illustrate the variation in peak frequency recorded between different stations. At Station 2, a resonance around 200 Hz is also observed, which could correspond to excitation in a thin playa layer around 1-2 m thick. **C)** Particle motion, with the N wave shown in orange (14:46:04.4 - 14:46:04.8 UTC) and the remainder of the wavetrain in blue.

Finally, Fig. 3**C)** shows the ground particle motion associated with the initial N-wave (orange) and the rest of the wavetrain (blue). The overwhelmingly vertical motion associated with the N-wave is clear. A potential elliptical polarisation can be seen in the rest of the wavetrain, suggesting the presence of Rayleigh waves here.

Slowness and origin azimuth

In considering the passage of the sonic boom over the array, it is important to consider that the capsule does not act as a point source. Rather, whilst travelling at supersonic speeds it is more appropriately described as a line source producing a conical shock front (Carlson and Maglieri, 1972). The opening angle of the cone, μ, is given by:

$$\mu = arcsin\frac{1}{M} \tag{1}$$

where M is the Mach number, in this case 30 – corresponding to an opening angle of 1.9°. This narrow Mach cone means that the seismic source may effectively be considered to be a cylinder (Karakostas et al., 2018). The acoustic rays themselves are emitted at the complement of the Mach angle (Cates and Sturtevant, 2002), which in this case is 88.1°, i.e., nearly normal to the shock front.

The intersection of the Mach cone with the ground produces a hyperbola along which a sonic boom is audible, and the passage of the hyperbola over the surface sweeps out a sonic boom 'carpet'. As per Eqn. 1, the hyberbolic footprint also becomes narrower with increasing Mach number.

In Figure 4, we first show the results of a beampack aimed at determining the 2D slowness of the overpressure wavefront, followed by vespagrams showing beams in slowness s_x and s_y space. These are constructed under the assumption that the wave propagates across the array as a plane wave at consistent velocity. We do not find it necessary to compensate for the small variation in topographic elevation across the array as this is < 4 m across an array aperture of ~ 600 m and hence the impact of elevation variation is small.

The beampack shows the maximum arrival amplitude with a 0.025 s window around the overall maximum amplitude stack, as a function of slowness in east (s_x) and north (s_y) directions. As Figure 4**A,B)** shows, there is a clear peak in amplitude associated with wavefront arrival at a slowness of $[s_x, s_y]$ = [-0.209, -0.063]. The actual signal is convolved with an array response function leading to amplitude artefacts associated with the orientation of the arms of the array in the uprange and crossrange directions, these are visible as bright lines in the beampack. The fact that the array response function passes slightly northwest of [0,0] in slowness space indicates the array was slightly to the south of the actual re-entry trajectory (consistent with pre-landing predictions, and indicating that the spacecraft was either on or ever so slightly south of its nominal re-entry line).

The 2D slowness of the wavefront arrival indicates that the point of apparent wavefront emission is at an azimuth of 253° (roughly WSW), and an apparent slowness of 0.214 s/km. The derived azimuth is very close to the pre-landing nominal prediction of 249°. The beampack is extremely well resolved, given the frequency of the overpressure wave and array aperture.

The vespagrams in Figure 4**C,D)** show evidence for either a slight variation in slowness across the array, or equivalently, the detection of wavefront curvature. In this case, where source-array distance is likely to be only around two orders of magnitude higher than the array aperture, slight wavefront curvature is more likely than the impact of a consistent atmospheric gradient on the lengthscale of the array aperture. The latter would also be expected given that the sonic boom footprint on the ground is a hyperbola.

Source location analysis

Given the azimuth and slowness resolution of the array, we are also able to estimate origin location of the shockwave. Without a full atmospheric model and inversion of the data, which are beyond the scope of this paper, this involves making a number of assumptions.

Firstly, we assume that the sonic boom can be represented as a plane wave propagating through the atmosphere, which, as we justify above, is an approximation which is reasonable in the far-field. Secondly, we assume that the shockwave has decayed sufficiently such that it propagates at the speed of sound v_0, which we calculate to be 332 m/s (see *Weather* section for more details on this calculation).

Geometrically, we consider the apparent slowness ($s_{app} = \frac{1}{v_{app}}$) of the wavefront across the array (e.g. Rost and Thomas (2002)) as:

$$s_{app} = \frac{sin\theta}{v_0} \tag{2}$$

In the downrange direction, the apparent velocity v_{app} of the wavefront across the array is 4,581 m/s. Note that this is an apparent, rather than physical, velocity and yields an estimated angle of emission which is 4.15° from the vertical. This is the equivalent point-source angle of emission, and does not reproduce the actual, extended-line source nature of the capsule as a seismic source; but it does indicate that the signal was produced almost exactly overhead the array, as expected. When combined with the derived bearing from the previous section of 253°, this indicates an origin for the shockwave which is slightly to the south-west of the array and almost vertically above it. Note that this result also suggests that the effects of atmospheric refraction of the acoustic rays is minimal, as each different layer of the vertically stratified atmosphere is encountered at a near-normal angle to its interface.

Pre- and post-cursors

Similarly to Fernando et al. (2024), no clear pre-cursor phases are noted, and there are no coherent sources detected by our array. This is as expected, because pre-cursors are normally restricted to settings where the supersonic source is 'slow' as compared to the compressional speed in the ground, such that surface waves induced immediately beneath the source can 'overtake' a slower direct airwave due to the higher wave speeds in the ground (Cook and Goforth, 1970). In this case, the

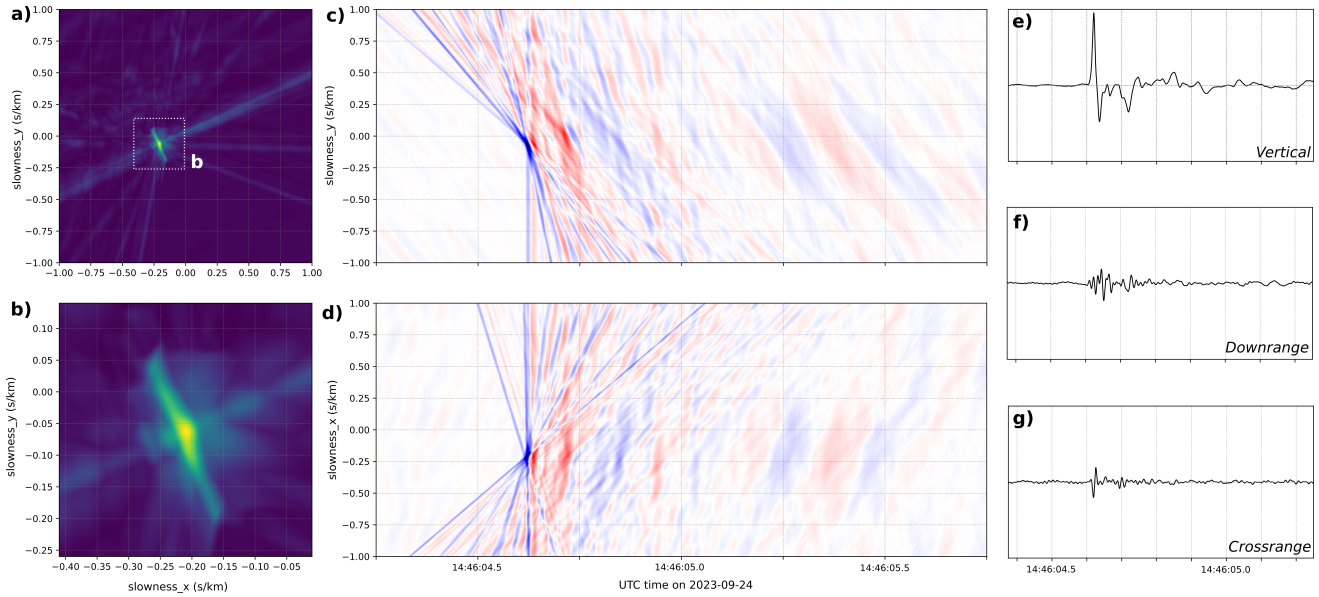

Figure 4. Array analysis of the ORX re-entry signal. **(a)** and **(b)** show the results of a beampack through slowness in x and y, taking the maximum amplitude with +/- 50 samples (0.025 seconds) of the absolute maximum amplitude for the shockwave arrival (at 14:46:04.621 and at a slowness of [-0.209, -0.063]). **(c)** and **(d)** show vespagrams in y and x slowness space, respectively. In each vespagram, the other slowness is fixed at the value giving the absolute maximum amplitude for the shockwave arrival. All plots are normalised to the peak value. **(e)-(g)** show the optimal-slowness beam for vertical, downrange and crossrange components, respectively in the pass band 1 – 100 Hz. All beams are normalised to the peak value of the vertical component beam.

capsule's velocity is very much greater than V_p, thus explaining the absence of pre-cursor phases (McDonald and Goforth, 1969). Furthermore, the sound speed in the ground is only slightly higher (less than factor 2) than the sound speed in the air.

We do note that there is an increase in noise levels around 14:45:50 UTC, around twenty seconds before the ORX signal (see *Traffic* section for more details). We exclude this as being a pre-cursor, as it arrives too early as compared to the airwave and has a move-out consistent with a vehicular origin, specifically a lorry/truck that arrived at the nearby rest area and idled until 14:47 UTC.

Conversely, a relatively rich set of seismic waves is apparent immediately after the initial rounded N-wave. These are visible as an extended set of oscillations in Figs. 2**A) and B)**. These have similar slowness to the airwave arrival, and hence are potentially associated with acoustic waves propagating in the atmosphere after the initial compression/rarefaction, or longer-duration complex deformation associated with the wavefront's passage over the station. It is also likely that Rayleigh waves are present in this wavetrain. Given that V_s in playa is extremely close to the sound-speed in air, the air-to-ground coupling should be strong. However, this closeness of speeds also makes phase separation challenging.

Comparison to known flight parameters

In theory, the detailed seismic recordings made at this array could be inverted for the capsule's trajectory and flight parameters. However, this is extremely challenging in practice, due to the lack of an exact atmospheric state model or an as-flown trajectory.

Nonetheless, we note that a comparison of the boom duration (τ) to theoretical predictions given by Kanamori et al. (1992) is possible. Following the approach of Whitham (1974) (though with slightly different notation, and correction for a missing exponent noted by Kanamori et al. (1992)), given a capsule speed u at height h we expect τ to be approximately given by:

$$\tau \approx \frac{2\sqrt{2k_2}k_3 h^{\frac{1}{4}}}{u} \tag{3}$$

where k_2 is a constant dependent on the ratio of specific heats within the atmosphere γ and the Mach number M:

$$k_2 = \frac{(\gamma+1)M^4}{\sqrt{2}(M^2-1)^{\frac{3}{4}}} \tag{4}$$

and k_3 is a constant related to the capsule's geometry,

$$k_3 = \delta l^{\frac{3}{4}} \tag{5}$$

where δ is the ratio of maximum effective capsule radius to capsule length l.

For the ORX capsule with radius 0.4 m and length 0.5 m, $k_3 = 0.48$ (noting that in practice, the effective radius of the capsule may be larger due to shockwave stand-off).

Given the nominal pre-landing predictions of $h = 62{,}000$ m and $u = 10{,}800$ m/s, and assuming a canonical $\gamma = 1.4$ (as per Kanamori et al. (1992), though it is likely lower at M = 30), we derive $k_2 \approx 8{,}370$. Using the 'effective' (slant) height makes little difference to this calculation given that the capsule is almost directly overhead.

These results yield an estimate of $\tau = 0.18$ s. This is in remarkably close agreement with our measured value of 0.15 s given the significant simplifications made in the calculation of the constants above and the unknown capsule height and atmospheric conditions at the time of overflight. Calculation of a more accurate ratio of specific heats or applying a correction for atmospheric structure and wind structure may enable an even more accurate match.

Kanamori et al. (1992) also gives an approximate relation for theoretical overpressure as a function of aspect ratio and altitude:

$$\frac{\Delta P}{P} \approx k_1 k_3 h^{-\frac{3}{4}} \tag{6}$$

Where k_1 is another constant given by:

$$k_1 = \frac{2^{\frac{1}{4}}\gamma}{(\gamma+1)^{\frac{1}{2}}}(M^2-1)^{\frac{1}{8}} \tag{7}$$

We compute $k_1 = 2.5$ and hence $\frac{\Delta P}{P} = 0.00030$. Based on a receiver altitude of 1,920 m and an ambient air temperature of +4.5°C, P = 79,600 Pa and hence $\Delta P \approx 24$ Pa. We are not able to directly compare this to the actual overpressure as the ground compliance at the array site was not measured.

However, we note that the the theoretical overpressure is still significantly larger than that recorded by Fernando et al. (2024) of 0.7 Pa at the Fish Creek site approximately 50 km away. Computing the expected overpressure at Fish Creek whilst

TABLE 1.
Meteorological data recorded by the Nevada Department of Transport Weather Station at US 50 Bean Flats Rest Area at 14:46:00 UTC. Data are shared as provided, surface temperature has been averaged over two sensors.

Variable	Value
Air temperature	+4.5°C
Surface temperature	+8.2°C
Dewpoint	-3.3°C
Relative humidity	56%
Wind direction	302°
Wind speed	0.0 m/s
Gust direction	291°
Gust speed	0.22 m/s
Precipitation	None

accounting for the longer slant height at this laterally offset station yields a predicted overpressure of 21 Pa, still around 30 times too large.

Therefore, we conclude that this formula for ΔP is not valid in this regime. This may due to the capsule's hypersonic speed producing a substantially modified bow shock, or its extreme altitude producing different interactions with the surrounding airflow, as compared to tests conducted at lower altitudes and lower Mach numbers.

Ancillary data

We will briefly discuss ancillary data which was collected as part of this deployment by part of a team of volunteers, working remotely with data provided online by the Nevada Department of Transport (NVDOT). All of this data, and similar readings from nearby potentially of interest to other portions of the ORX EDL instrumentation campaign, are available in our online repository (see Data and Resources section for link).

Weather data

The proximity of the array to US Highway 50 ('The Loneliest Road in America') had the advantage that meteorological data could be sourced from a nearby NVDOT weather station. This station ('US50 Bean Flats Rest Area') was only 275 m from the array centrepoint. The closest reading to the capsule's overflight and the arrival of the sonic boom was made at 14:44:00 UTC, with measurements shown in Table 1.

Whilst the lack of wind during this period represents only a single measurement at the surface, it may be indicative of a quiescent planetary boundary layer at the time in question. This may have led to less turbulent dissipation of the wavefront (one of the sources of rounding in the N-wave).

TABLE 2.
Traffic data recorded by the cameras at the US 50 Bean Flat Rest Area. Note that 'Away' and 'Towards' refer to whether the vehicle was moving away from (westbound) or towards (eastbound) relative to the westward-facing traffic camera. Speeds were judged by each individual relative to the average in the 30 minutes or so preceeding the interval of interest

UTC Time - Lower Bound	UTC Time - Mean	UTC Time - Upper Bound	Direction	Speed	Type
14:39:26	14:39:47	14:40:03	Away	Medium/Fast	Car
14:41:23	14:41:35	14:41:53	Towards	Medium	Car (with trailer?)
14:41:38	14:41:39	14:41:39	Towards	Medium	Car (with trailer?)
14:47:49	14:47:57	14:48:00	Away	Slow/stationary	Lorry/truck
14:51:47	14:51:52	14:52:00	Towards	Medium/Slow	Car with trailer

Traffic data

We also made use of the traffic camera installed at the Bean Flats Rest area to record traffic movements, with the aim of being able to identify contamination in the ORX signal if needed.

Data for around five minutes before and after the overflight are given in Table 2. Because the traffic camera feeds are not archived, multiple volunteers were asked to record vehicles passing the array in real time, thereby eliminating some of random the error associated with streaming lag (we find a systematic error of around 40 s delay in video data as compared to when a vehicle becomes apparent in the seismic data). The data provided is a synthesis of that from all volunteers, with the lower, mean, and upper bounds on vehicle passage times given. The streaming lag has not been corrected for in Fig. 2.

In two cases, the vehicle may have been towing a trailer, but this could not be determined due to poor video resolution. In order to corroborate readings between different volunteers who recorded slightly different vehicle arrival times due to streaming lag, car colour was also recorded – but this is not noted in Table 2 as it is not relevant to seismic observations.

As per Table 2, no moving vehicles were noted at 14:46 UTC, when the ORX signal was detected. A truck which passed the camera at 14:47 UTC was identified in the seismic dataset as being a source of noise beginning at 14:45:50 UTC, and extending out to 14:49 UTC. Given this long duration, and its slow speed observed in the video data, we suspect it was idling in the layby prior to driving away.

Summary

Seismic signatures associated with the EDL of the OSIRIS-REx spacecraft were recorded by an 11-instrument seismic array located almost immediately under the point of peak heating over northern Nevada.

A classic rounded N-wave, characteristic of a decayed sonic boom, is observed propagating across the array. The entire N-wave (compression and rarefaction) lasts approximately 0.15 s, with the compressional wave extending to higher frequencies (up to at least ~450 Hz at some stations) than the rarefaction (~40 Hz). The measured duration of the N-wave is in very good agreement with theoretical predictions.

The wavefront's moveout across the array is predominantly in the downrange direction (at an azimuth of 253°, close to the pre-landing prediction of 249°. The wave is also propagating almost vertically downward (around 4° from the vertical). Following the N-wave, a set of seismic post-cursors are recorded, likely some combination of air-coupled seismic waves, additional (slower) airwaves, and long-period ground deformation induced by the initial wavefront.

Data from this array are able to exclude the spacecraft being well south of its nominal trajectory. Analysis of the apparent slowness of the N-wave across the array also indicates an equivalent point-source origin which is almost exactly overhead in both the uprange-downrange and crossrange planes.

Further work would likely enable a more thorough inversion of the capsule's trajectory, accounting for the extended nature of the source and the effects of refraction arising from atmospheric stratification. This would enable this dataset to be used as a more reliable test-case for trajectory determinations of natural meteoroids using their seismic signatures.

Data and Resources

Deployment locations and ancillary data (weather and traffic data) are available via in this Zenodo repository: https://doi.org/10.5281/zenodo.12210877. Seismic data are available from the FDSN under network code 2X (Benjamin A. Fernando et al., 2023) at DOI 10.7914/8ZEK-PE59.

Declaration of Competing Interests

The authors acknowledge that there are no conflicts of interest recorded.

Acknowledgments

The authors are most grateful to NASA's Scientifically Calibrated In-Flight Imagery (SCIFLI) team for facilitating the fieldwork component of this expedition and to the townspeople of Eureka, Nevada for their hospitality. They are also grateful to NVDOT for the free access to traffic and meteorological data.

BF is funded by the Blaustein Fellowship in Earth and Planetary Sciences at Johns Hopkins University. JW was funded by the Miller Institute for Basic Research in Science at UC Berkeley. CC is funded by the UK Space Agency Fellowship in Mars Exploration Science under ST/Y005600/1. TC thanks the Royal Society for funding under URF\R\231019.

References

Ajluni, T., D. Everett, T. Linn, R. Mink, W. Willcockson, and J. Wood (2015). OSIRIS-REx, returning the asteroid sample. In *2015 IEEE aerospace conference*, pp. 1–15. IEEE.

Allander, K. K. and D. L. Berger (2009). Seismic velocities and thicknesses of alluvial deposits along Baker Creek in the Great Basin National Park, east-central Nevada. Technical report, U. S. Geological Survey.

Ben-Menahem, A. and S. J. Singh (1981). *Seismic waves and sources*. Springer Science & Business Media.

Benjamin A. Fernando, Constantinos Charalambous, and Nicholas Schmerr (2023). Array-based seismic measurements of osiris-rex's re-entry.

Carlson, H. W. and D. J. Maglieri (1972). Review of sonic-boom generation theory and prediction methods. *The Journal of the Acoustical Society of America* **51**(2C), 675–685.

Cates, J. E. and B. Sturtevant (2002). Seismic detection of sonic booms. *The Journal of the Acoustical Society of America* **111**(1), 614–628.

Cook, J. C. and T. T. Goforth (1970). Ground motion from sonic booms. *Journal of Aircraft* **7**(2), 126–129.

Edwards, W. N., D. W. Eaton, and P. G. Brown (2008). Seismic observations of meteors: Coupling theory and observations. *Reviews of Geophysics* **46**(4).

Fernando, B., C. Charalambous, C. Saliby, E. Sansom, C. Larmat, D. Buttsworth, D. Hicks, R. Johnson, K. Lewis, M. McCleary, et al. (2024). Seismoacoustic measurements of the OSIRIS-REx re-entry with an off-grid Raspberry PiShake. *Seismica* **3**(1).

Fernando, B., N. Wójcicka, M. Froment, R. Maguire, S. C. Stähler, L. Rolland, G. S. Collins, O. Karatekin, C. Larmat, E. K. Sansom, et al. (2021). Listening for the landing: Seismic detections of Perseverance's arrival at Mars with InSight. *Earth and Space Science* **8**(4), e2020EA001585.

Fernando, B., N. Wójcicka, Z. Han, A. Stott, S. Ceylan, C. Charalambous, G. S. Collins, D. Estévez, M. Froment, M. Golombek, et al. (2021). Questions to Heaven. *Astronomy & Geophysics* **62**(6), 6–22.

Fernando, B., N. Wójcicka, R. Maguire, S. C. Stähler, A. E. Stott, S. Ceylan, C. Charalambous, J. Clinton, G. S. Collins, N. Dahmen, et al. (2022). Seismic constraints from a Mars impact experiment using InSight and Perseverance. *Nature Astronomy* **6**(1), 59–64.

Kanamori, H., J. Mori, B. Sturtevant, D. Anderson, and T. Heaton (1992). Seismic excitation by space shuttles. *Shock waves* **2**, 89–96.

Karakostas, F., V. Rakoto, P. Lognonne, C. Larmat, I. Daubar, and K. Miljković (2018). Inversion of meteor rayleigh waves on earth and modeling of air coupled rayleigh waves on mars. *Space Science Reviews* **214**, 1–33.

Kenda, B., M. Drilleau, R. F. Garcia, T. Kawamura, N. Murdoch, N. Compaire, P. Lognonné, A. Spiga, R. Widmer-Schnidrig, P. Delage, V. Ansan, C. Vrettos, S. Rodriguez, W. B. Banerdt, D. Banfield, D. Antonangeli, U. Christensen, D. Mimoun, A. Mocquet, and T. Spohn (2020). Subsurface structure at the insight landing site from compliance measurements by seismic and meteorological experiments. *Journal of Geophysical Research: Planets* **125**(6).

McDonald, J. A. and T. T. Goforth (1969). Seismic effects of sonic booms: Empirical results. *Journal of Geophysical Research* **74**(10), 2637–2647.

Pierce, A. D. and D. J. Maglieri (1972). Effects of atmospheric irregularities on sonic-boom propagation. *The Journal of the Acoustical Society of America* **51**(2C), 702–721.

Plotkin, K. J. (2002). State of the art of sonic boom modeling. *The Journal of the Acoustical Society of America* **111**(1), 530–536.

ReVelle, D. and W. Edwards (2007). Stardust—an artificial, low-velocity "meteor" fall and recovery: 15 January 2006. *Meteoritics & Planetary Science* **42**(2), 271–299.

ReVelle, D., W. Edwards, and T. Sandoval (2005). Genesis—an artificial, low velocity "meteor" fall and recovery: September 8, 2004. *Meteoritics & Planetary Science* **40**(6), 895–916.

Rost, S. and C. Thomas (2002). Array seismology: Methods and applications. *Reviews of geophysics* **40**(3), 2–1.

Sansom, E. K., H. A. Devillepoix, M.-y. Yamamoto, S. Abe, S. Nozawa, M. C. Towner, M. Cupák, Y. Hiramatsu, T. Kawamura, K. Fujita, et al. (2022). The scientific observation campaign of the Hayabusa-2 capsule re-entry. *Publications of the Astronomical Society of Japan* **74**(1), 50–63.

Silber, E. A., D. C. Bowman, and S. Albert (2023). A review of infrasound and seismic observations of sample return capsules since the end of the Apollo era in anticipation of the OSIRIS-REx arrival. *Atmosphere* **14**(10), 1473.

Silber, E. A., D. C. Bowman, C. G. Carr, D. P. Eisenberg, B. R. Elbing, B. Fernando, M. A. Garcés, R. Haaser, S. Krishnamoorthy, C. A. Langston, et al. (2024). Geophysical observations of the 24 September 2023 OSIRIS-REx sample return capsule re-entry. *arXiv preprint arXiv:2407.02420*.

Sorrells, G. G. (1971). A preliminary investigation into the relationship between long-period seismic noise and local fluctuations in the atmospheric pressure field. *Geophysical Journal of the Royal Astronomical Society* **26**(1-4), 71–82.

Whitham, G. B. (1974). *Linear and nonlinear waves*. John Wiley & Sons.

Yamamoto, M.-y., Y. Ishihara, Y. Hiramatsu, K. Kitamura, M. Ueda, Y. Shiba, M. Furumoto, and K. Fujita (2011). Detection of acoustic/infrasonic/seismic waves generated by hypersonic re-entry of the HAYABUSA capsule and fragmented parts of the spacecraft. *Publications of the Astronomical Society of Japan* **63**(5), 971–978.

Author affiliations

(BF, KL, LEH, SK, CP) Department of Earth and Planetary Sciences, Johns Hopkins University, 3400 N Charles St, Baltimore, Maryland, 21218, United States (CC) Department of Electrical and Electronic Engineering, Imperial College London, London, United Kingdom (NS) Department of Geology, University of Maryland, College Park, Maryland, 20742, United States (TC) Institute of Geophysics and Tectonics, School of Earth and Environment, University of Leeds, Leeds, United Kingdom (JW) Department of Earth and Planetary Sciences, University of California, Berkeley, California, 94720, United States; Miller Institute for Basic Research in Science, Berkeley, California, 94720, United States (ES, HD) International Centre for Radio Astronomy Research, Space Science and Technology Centre, Curtin University, Perth, Western Australia, Australia (ES) Space Science and Technology Centre, School of Earth and Planetary Science, Curtin University, Perth, Australia (CS) Observatoire de la Côte d'Azur, Université Côte d'Azur, CNRS, IRD, Géoazur, Valbonne, France (MM) Analytical Mechanics Associates, Inc./NASA Langley Research Center, Hampton, Virginia, 23681, United States (JI) NASA Langley Research Center, Hampton, Virginia, 23681, United States (JL) Sandia National Laboratories, Albuquerque, New Mexico, 87185, United States (MRG) Department of Earth Sciences, Southern Methodist University, Dallas, Texas, 75275, United States (KP) Independent Researcher, Bowie, Maryland, 20715, United States (MF) Sandia National Laboratories, Albuquerque, New Mexico, 87185, United States (CL) Los Alamos National Laboratory, Los Alamos, New Mexico, 87545, United States (OK) Royal Observatory of Belgium, Uccle, Belgium (SB) Independent Researcher, Boulder, Colorado, 80304, United States (DB, FZ) Institute for Advanced Engineering and Space Sciences, University of Southern Queensland, Queensland, Australia (JC) Department of Geological Sciences, University of Alabama, Tuscaloosa, Alabama, 35487, United States (NC) University of Western Ontario, London, Ontario, Canada (LD) School of Geographical and Earth Sciences, University of Glasgow, Glasgow, United Kingdom (AMG) Institute of Space Science and Technology, University of Karachi, Karachi, Pakistan (CTG) Archaeology, Environmental Changes & Geo-Chemistry, Vrije Universiteit Brussel, Brussels, Belgium (H) Laboratory

368 for Atmospheric and Space Physics, University of Colorado, Boulder, Colorado, 80303, United States (DCH) United States
369 Department of Defense (KBR Consultant), Las Cruces, New Mexico, 88001, United States (RJ) NASA Ames Research
370 Center, Moffett Field, California, 94035, United States (SNL) Earth, Energy, and Environment Centre, University of Kansas,
371 Lawrence, Kansas, 66045, United States (TR) Atominstitut, Technische Universität Wien, Vienna, Austria (LR) Laboratoire
372 Géoazur - Université de Nice Côte d'Azur (MMT) Department of Geosciences, University of Edinburgh, Edinburgh, Scotland
373 (ART) Institute for Geophysics, University of Texas, Austin, Texas, 78712, United States

Figure Legends

Figure 1: Top panel: the ORX EDL trajectory (side view), from the point of atmospheric interface to landing. Bottom panel: geographical context (top-down view) of the trajectory. We refer to directions towards landing as 'downrange' and those towards atmospheric interface as 'uprange'. The inset panel shows the seismometer array deployment. Note that the long arm of the array is parallel to the expected trajectory (i.e. runs uprange/downrange). The cross arm is perpendicular to the trajectory (i.e. crossrange). The lateral distance between the centre-line of the array and the trajectory footprint on the ground is approximately 2300 m.

Figure 2: Seismic data recorded by the array. Traces are vertical ground velocity in the 1-100 Hz range and are arranged in **A)** by downrange distance from the westernmost station in the array and in **B)** by crossrange distance from the northernmost station. Station numbers are indicated in red on the left hand side. The weak signal at station 4 is thought to be due to issues with the instrument, which displayed higher noise levels throughout the deployment.

Figure 3: Data from the central station of the array (Station 1), bandpassed between 1 and 100 Hz. The N-wave is only clearly apparent on the vertical component. **A)** Three-component data, showing the dominance of the signal on the vertical component. **B)** Velocity spectrogram for the vertical component. A small inset is shown for Station 2 (one station uprange from Station 1), to illustrate the variation in peak frequency recorded between different stations. At Station 2, a resonance around 200 Hz is also observed, which could correspond to excitation in a thin playa layer around 1-2 m thick. **C)** Particle motion, with the N wave shown in orange (14:46:04.4 - 14:46:04.8 UTC) and the remainder of the wavetrain in blue.

Figure 4: Array analysis of the ORX re-entry signal. **(a)** and **(b)** show the results of a beampack through slowness in x and y, taking the maximum amplitude with +/- 50 samples (0.025 seconds) of the absolute maximum amplitude for the shockwave arrival (at 14:46:04.621 and at a slowness of [-0.209, -0.063]). **(c)** and **(d)** show vespagrams in y and x slowness space, respectively. In each vespagram, the other slowness is fixed at the value giving the absolute maximum amplitude for the shockwave arrival. All plots are normalised to the peak value. **(e)-(g)** show the optimal-slowness beam for vertical, downrange and crossrange components, respectively in the pass band 1 – 100 Hz. All beams are normalised to the peak value of the vertical component beam.

Manuscript Received Manuscript Received 22112024